applied sciences

MDPI

Article

Robust and Unbiased Estimation of Robot Pose and Pipe Diameter for Natural Gas Pipeline Inspection Using 3D Time-of-Flight (ToF) Sensors

Hoa-Hung Nguyen [1], Jae-Hyun Park [1], Jae-Jun Kim [2], Kwanghyun Yoo [2], Dong-Kyu Kim [2] and Han-You Jeong [3,*]

[1] School of Electrical and Electronics Engineering, Pusan National University, Busan 46241, Republic of Korea; nguyenhoahungit@gmail.com (H.-H.N.); popwogus@gmail.com (J.-H.P.)
[2] Robotic In-Line Inspection Research Team, Trunk Line Operation Department, Korea Gas Corporation (KOGAS), Incheon 21993, Republic of Korea; jaejunkim@kogas.or.kr (J.-J.K.); khyoo@kogas.or.kr (K.Y.); dongkyukim@kogas.or.kr (D.-K.K.)
[3] School of Electrical and Electronics Engineering, and Robotics Institute of Non-Destructive In-Line Inspection (RiNDi), Pusan National University, Busan 46241, Republic of Korea
* Correspondence: hyjeong@pusan.ac.kr; Tel.: +82-51-510-7332

Abstract: The estimation of robot pose and pipe diameter is an essential task for reliable in-line inspection (ILI) operations and the accurate assessment of pipeline attributes. This paper addresses the problem of robot pose and pipe diameter estimation for natural gas pipelines based on 3D time-of-flight (ToF) sensors. To tackle this challenge, we model the problem as a non-linear least-squares optimization that fits 3D ToF sensor measurements in its local coordinates to an elliptic cylindrical model of the pipe inner surface. We identify and prove that the canonical ellipse-based estimation method (C-EPD), which uses a canonical residual function, suffers from bias in diameter estimation due to its asymmetry to depth errors. To overcome this limitation, we propose the robust and unbiased estimation of pose and diameter (RU-EPD) approach, which employs a novel error-based residual function. The proposed function is symmetric to depth errors, effectively reducing estimation bias. Extensive numerical simulations and prototype pipeline experiments demonstrate that RU-EPD outperforms C-EPD, achieving an at least six times lower estimation bias and a 2.5 times smaller estimation error range in pipe diameter and about a 2 times smaller estimation error range in pose estimation.

Keywords: in-line inspection; in-pipe robot; pose estimation; pipe diameter estimation; estimation bias; depth error

Academic Editor: Enbin Liu, Hongfang Lu, Weibiao Qiao and Shanbi Peng

Received: 14 January 2025
Revised: 11 February 2025
Accepted: 13 February 2025
Published: 17 February 2025

Citation: Nguyen, H.-H.; Park, J.-H.; Kim, J.-J.; Yoo, K.; Kim, D.-K.; Jeong, H.-Y. Robust and Unbiased Estimation of Robot Pose and Pipe Diameter for Natural Gas Pipeline Inspection Using 3D Time-of-Flight (ToF) Sensors. *Appl. Sci.* **2025**, *15*, 2105. https://doi.org/10.3390/app15042105

1. Introduction

Pipeline systems are critical infrastructures used to transport liquids and gases over long distances. Maintaining their integrity is essential to prevent failures that may lead to environmental damage and economic losses [1–3]. In-line inspection (ILI) plays a vital role in ensuring pipeline safety by identifying corrosion, cracks, and deformation [1,2]. ILI utilizes an in-pipe robot equipped with various sensors, such as magnetic flux leakage, ultrasonic, electromagnetic acoustic transducer, caliper, and optical sensors, to record the pipe condition and navigate through the pipeline effectively [2,4].

Two key functions of ILI robots are estimating their pose and measuring pipe diameter. Pose estimation refers to the estimation of the orientation and displacement of the robot inside the current pipe. It is different from the well-studied localization problem which finds the global location along the pipeline [5]. Accurate pose estimation is essential for precise robot control and spatial alignment during inspection. In addition to pose estimation, accurately determining pipe diameter is equally critical for ensuring inspection precision and assessing structural integrity. Diameter estimation addresses pipe deformations caused by manufacturing imperfections or non-uniform external pressures. Pipes are often approximated as elliptic cylinders, and diameter estimation involves measuring the major- and minor-axis lengths of their elliptical cross-sections. Pipe diameter serves as a key indicator of structural deformation and supports the calibration of sensor measurements with respect to orientation, displacement, and pipe geometry. The accurate estimation of robot pose and pipe diameter not only supports effective inspection but also improves robot control and sensor calibration, which are the main focus of this paper.

To estimate robot pose and pipe diameter, existing approaches rely on structured light, 2D cameras, and stereo cameras. The first approach relies on analyzing the deformation of a light pattern to compute either robot pose or pipe diameter [6–11]. This approach does not fully estimate robot pose and pipe diameter due to the lack of depth information. The second approach applies visual odometry on consecutive images from a 2D camera to determine robot pose [12,13]. It relies on features extracted from the pipe inner surface. However, these features may become unclear or unreliable due to lighting conditions, dust, or reflective surfaces inside the pipeline, leading to matching errors and pose estimation failures. The third approach relies on a system of multiple stereo cameras [14,15]. However, this method requires high processing costs for multiple cameras and also needs multiple frames to estimate robot pose and pipe diameter. On the other hand, 3D time-of-flight (ToF) sensors, such as lidar [16] or 3D ToF cameras [17], can preserve the full geometry of the pipe without requiring feature extraction or multi-frame processing. Therefore, we focus on solving the estimation problem using a single frame from a single 3D ToF camera.

Despite their advantages compared to other approaches, 3D ToF sensors are susceptible to depth errors caused by factors such as infrared modulation inaccuracies, integration time variations, and temperature changes [18]. These errors are generally classified into outliers, depth biases, and random depth errors [19–22]. While outliers can be removed by clustering the data [22] and depth biases can be compensated through sensor calibration [19,20], random depth errors are typically corrected only for standstill sensors [21]. Although random depth errors may appear less significant, their impact on precision-demanding applications such as robot pose and pipe diameter estimation can result in substantial inaccuracies and inconsistencies. This paper specifically addresses the effect of random depth errors in the estimation of robot pose and pipe diameter.

In this paper, we propose robust and unbiased estimation of robot pose and pipe diameter (RU-EPD). RU-EPD is based on our novel error-based residual function which estimates robot pose and pipe diameter robustly and unbiasedly. We first formulate an estimation of robot pose and pipe diameter as a non-linear least-square fitting problem with the canonical ellipse residual function (C-EPD). It transforms sensor measurements from the sensor coordinate system to the pipe coordinate system and fits the transformed points to an elliptic cylinder model evaluated by the canonical ellipse residual function. We analyze and prove that C-EPD produces an estimation bias in pipe diameter estimation with this residual function and the presence of random depth errors. The canonical ellipse residual function is more sensitive to positive depth errors than negative depth errors which leads to the overestimation of pipe diameter. To overcome this limitation, we propose a novel error-based residual function for RU-EPD. This function directly estimates depth errors and eliminates the asymmetry inherent in the canonical residual function. We mathematically prove that the error-based residual function ensures an unbiased estimation of pipe diameter. Extensive simulations and prototype pipeline experiments validate that RU-EPD successfully corrects the estimation bias of C-EPD. Furthermore, RU-EPD demonstrates significantly higher consistency in both robot pose and pipe diameter estimation, proving its robustness against sensor measurement noise.

The contributions of this paper are summarized as follows:

- We identify and mathematically prove the estimation bias introduced by C-EPD due to its canonical ellipse residual function.
- We propose a novel error-based residual function for RU-EPD, which eliminates asymmetry to depth errors and ensures robust and unbiased performance.
- Using both simulated and experimental results, we demonstrate that RU-EPD outperforms C-EPD, achieving higher accuracy and consistency in robot pose and pipe diameter estimation.

The remainder of this paper is organized as follows: Section 2 briefly summarizes related works on the estimation of robot pose and pipe diameter, as well as the depth error in 3D ToF sensors. Section 3 presents the RU-EPD scheme, including theoretical analysis and the proposed error-based residual function. The numerical results are presented and discussed in Section 4. Finally, we conclude this paper in Section 5, summarizing key findings and discussing potential directions for future research.

2. Related Works

This section reviews common approaches for estimating robot pose and pipe geometry, including structured light, 2D cameras, and stereo cameras. It also examines approaches to addressing depth errors in 3D ToF sensors, which are presented as a promising alternative for accurate and robust estimation.

2.1. Estimation of Robot Pose and Pipe Diameter

The accurate estimation of robot pose and pipe diameter is important in ILI. A robot pose, describing its orientation and displacement inside a pipe, is modeled with six degrees of freedom (DoFs) consisting of roll, pitch, yaw, and X-, Y-, and Z-axis displacements. Because X-axis displacement is typically measured using an odometer in most in-pipe robots [1,2,4,5], this paper focuses on a five-DoF pose excluding X-axis displacement. Modeled as an elliptic cylinder, the pipe diameter is defined by its major and minor axes. It is essential for detecting structural deformations caused by manufacturing imperfections or external pressures. These estimates are also critical for improving inspection accuracy. To tackle these challenges, various sensor-based approaches have been proposed: structured light [6–11], 2D cameras [12,13], and stereo cameras [14,15].

Structured light methods project patterns onto the pipe surface and analyze their deformations in 2D camera images to estimate the robot pose and pipe diameter. In [6], the authors propose a method to estimate two-DoF poses (pitch and yaw) using a hyperbolic mirror and point light pattern by analyzing the point location in the image. A later scheme in [7] introduces a ring-shaped light pattern to estimate four-DoF poses (pitch, yaw, Y-displacement, and Z-displacement) by matching observed rings with pre-collected image databases of known poses. The schemes in [8,9] reformulate the problem as a non-linear optimization task using ring-shaped light patterns. Additionally, a ring-shaped light is employed to estimate the pipe diameter by sampling the ring radius [10] or fitting the ring image with an ellipse [11]. However, this approach relies solely on 2D image analysis without capturing depth information, making it impossible to fully estimate five-DoF poses and pipe diameter.

The 2D camera approach applies visual odometry to estimate six-DoF poses, including X-displacement. Instead of analyzing a single image, this approach utilizes sequential images to overcome the lack of depth information. Hansen et al. propose a feature-based visual odometry algorithm that extracts and matches corner features between images, enabling incremental pose updates [12]. To improve accuracy, structured light with two points is added in [13]. However, this approach depends on surface features, which can be unclear due to lighting conditions or dust, leading to matching failures. Furthermore, drift errors accumulate over time due to inaccuracies in successive frame matching.

A more recent approach utilizes stereo cameras to reconstruct 3D point clouds of pipe surfaces. Shang et al. employed four stereo cameras to measure the pipe surface and estimate robot pose using visual odometry applied to 3D point clouds [14]. Although this method achieved higher accuracy than 2D approaches, it still relied on surface features and demanded multi-frame processing. To address these issues, Yang et al. proposed a multi-camera system that emulates four stereo cameras combined with a ring-shaped light [15]. The 3D point cloud is constructed by collecting ring light points across consecutive frames, and poses and diameters are estimated using non-linear cylinder fitting. Although this approach improves robustness, it requires rail-mounted setups for consistent pose alignment across frames and imposes high computational demands due to extensive calibration among multiple cameras.

While structured light, 2D cameras, and stereo camera systems provide viable solutions for robot pose and pipe diameter estimation, they face limitations such as feature dependency, multi-frame processing, and computational complexity. In contrast, 3D ToF sensors offer a practical and scalable alternative by capturing depth data directly in a single frame without relying on features or multi-frame alignment. Despite their advantages, 3D ToF sensors are prone to depth errors, including outliers, depth biases, and random depth errors, which can significantly affect estimation accuracy. These challenges and their correction methods are explored in detail in the next section.

2.2. Depth Errors in 3D ToF Sensors

Despite their advantages, 3D ToF sensors, such as lidar or 3D ToF cameras, are affected by various types of depth errors that can compromise the accuracy of pose and diameter estimation. Depth errors in 3D ToF sensors can be broadly categorized into outliers, depth biases, and random depth errors [19–22]. Outliers are caused by multipath interference or low reflectivity. Depth biases result from systematic errors such as modulation inaccuracies and result in systematic deviation from the ground-truth depth while random depth errors occur due to the thermal noise or low reflective surface that is usually approximated as zero-mean Gaussian distribution. To remove outliers, the authors in [22] utilized the density-based spatial clustering of applications with noise (DBSCAN) while estimating the robot pose. To correct the depth bias, the authors in [19] proposed a joint calibration scheme to calibrate a 2D camera and a 3D ToF camera based on the checkerboard. This scheme eliminates depth biases without requiring ground-truth measurements. In [20], a machine-learning approach to correcting the depth bias for ToF cameras is proposed. It combines a particle filter and support vector machine to learn and correct the distance-dependent depth bias. On the other hand, to correct the random depth error, Fang et al. [21] propose a correction scheme based on entropy-based multilayer perception. It is trained to correct the random depth error using multiple frames of the same scene and pose. Due to the continuous movement of the in-pipe robot, the scene as well as robot pose in the pipe also continuously changes. Therefore, this scheme is unsuitable for in-pipe robots. As a result, random depth errors remain a significant challenge for in-pipe robots, particularly in estimating robot pose and pipe diameter.

This paper investigates the impact of random depth errors on robot pose and pipe diameter estimation. This estimation problem is modeled as a non-linear least-squares optimization which transforms the measurement points from the sensor coordinate system to the pipe coordinate system and fits the transformed points to the elliptic cylinder model. The commonly used canonical ellipse residual function is shown to overestimate the pipe diameter in the presence of random depth errors, as it is more sensitive to positive errors than negative errors, leading to estimation bias. To address this, we propose a novel error-based residual function that explicitly estimates depth errors. Unlike the canonical approach, this function is symmetric to positive and negative errors, ensuring unbiased estimation. The details of these residual functions and their application to addressing random depth errors will be presented in the following section.

3. Our Approach to Estimation of Robot Pose and Pipe Diameter (EPD)

We first present a framework for robot pose and pipe diameter estimation modeled as a non-linear least-squares problem, where the cross-section is represented as an ellipse. C-EPD uses the canonical ellipse form directly as the residual function in the non-linear least-squares problem. We analyze and prove the estimation bias inherent in C-EPD caused by the canonical ellipse residual function. Finally, we propose a novel error-based residual function for RU-EPD.

3.1. Framework of Robot Pose and Pipe Diameter Estimation

The in-pipe robot is equipped with a 3D ToF sensor to capture depth measurements in its front area, as illustrated in Figure 1. The sensor collects N measurement points per frame in the sensor coordinate system (SCS), where the origin x_0 is located at the center of the sensor, and the X-, Y-, and Z-axes are aligned along its front, right, and upward directions, respectively. Due to deformations caused by manufacturing imperfections or external pressure, the pipe inner surface is modeled as a cylinder with its cross-section represented by an ellipse. In this model, the pipe diameter is characterized by the major-axis length ($D_{\max}$) and minor-axis length ($D_{\min}$).

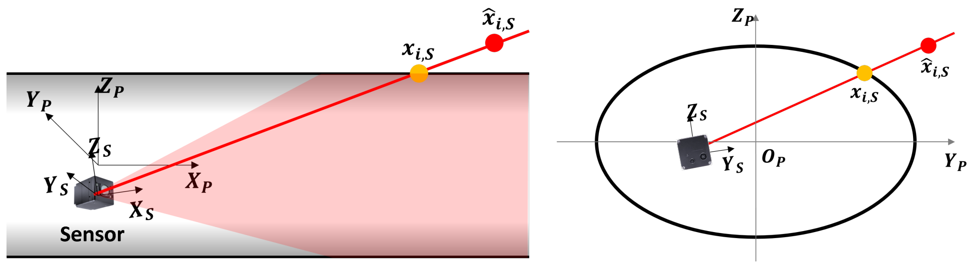

(**a**) Side view. (**b**) Cross-section view.

Figure 1. Illustration of measurement points collected by 3D ToF sensor. (**a**) Side view showing sensing line, measurement point $\hat{\boldsymbol{x}}_{i,S}$, and ground-truth point $\boldsymbol{x}_{i,S}$. (**b**) Cross-sectional view highlighting elliptical shape of pipe.

This paper addresses the problem of accurately estimating robot pose and pipe diameter based on measurements collected by a 3D ToF sensor. The sensor provides real-time measurements of the pipe inner surface in the SCS. Each measurement point represents the depth from the sensor origin to the pipe inner surface along a sensing line (red line). The measured point in the SCS is denoted by $\hat{\boldsymbol{x}}_{i,S} = [\hat{x}_{i,S}, \hat{y}_{i,S}, \hat{z}_{i,S}]^T$ $(1 \le i \le N)$. We assume that the sensor is well calibrated, effectively eliminating depth biases. Due to random depth errors, $\hat{\boldsymbol{x}}_{i,S}$ deviates irregularly from the ground-truth point $\boldsymbol{x}_{i,S}$ which represents the exact intersection between the sensing line and the pipe inner surface. Since the dispersion of the ToF camera light is extremely low, three points—$\boldsymbol{x}_0$, $\boldsymbol{x}_{i,S}$, and $\hat{\boldsymbol{x}}_{i,S}$—lie along the same sensing line. Then, the random depth error $\boldsymbol{\epsilon}_{i,S} = [\epsilon_{x,i,S}, \epsilon_{y,i,S}, \epsilon_{z,i,S}]^T$ can be modeled as

$$\boldsymbol{\epsilon}_{i,S} = \hat{\boldsymbol{x}}_{i,S} - \boldsymbol{x}_{i,S}. \tag{1}$$

If the measured point $\hat{\boldsymbol{x}}_{i,S}$ lies closer to the sensor origin than the ground-truth point $\boldsymbol{x}_{i,S}$, it is classified as a negative-error point ($|\hat{\boldsymbol{x}}_{i,S}| - |\boldsymbol{x}_{i,S}| < 0$). Conversely, if it lies farther away, it is classified as a positive-error point ($|\hat{\boldsymbol{x}}_{i,S}| - |\boldsymbol{x}_{i,S}| > 0$). For mathematical simplicity, we also assume that the signed depth error $\boldsymbol{\epsilon}_{i,S}$ follows a zero-mean Gaussian distribution $\mathcal{N}(0, \sigma_\epsilon^2)$, where each component of $\boldsymbol{\epsilon}_{i,S}$ is an independent and identically distributed (i.i.d.) Gaussian component with the standard deviation $1/\sqrt{3}\sigma_\epsilon$.

While the SCS effectively captures the cylinder-shaped structure of the pipe inner surface, it suffers from a key limitation: the axes in the SCS are defined based on the orientation of the robot, which varies dynamically with its pose. As a result, the pipe model represented by measurement points is pose-dependent, making it challenging to evaluate deviations of measurement points from the pipe model.

To address this challenge, we propose a stable reference coordinate system, called the pipe coordinate system (PCS), in which the X-axis aligns with the axial center of the pipe along the direction of robot movement, while the Y-axis and Z-axis correspond to the major and minor axes of the elliptical cross-section, respectively. This fixed orientation allows the decoupling of the pose from the pipe model and enables a geometrically meaningful representation of the pipe structure. The fundamental challenge is to transform the measurement points collected in the SCS into the PCS using a rigid transformation that accounts for the robot pose. This transformation involves rotations and translations that align the sensor measurements with the PCS axes.

The parameters governing this rigid transformation correspond to the quintuple robot pose in the PCS, denoted by $(\theta_x, \theta_y, \theta_z, \delta_y, \delta_z)$, where $(\theta_x, \theta_y, \theta_z)$ represents a three-axis rotation (roll, pitch, yaw) and (δ_y, δ_z) represents a translation along the Y- and Z-axes, which align with the pipe's major and minor axes, respectively. Combining these pose parameters with the pipe's major- and minor-axis lengths yields a septuple-parameter vector, as follows:

$$\boldsymbol{\beta} = (D_{\max}, D_{\min}, \theta_x, \theta_y, \theta_z, \delta_y, \delta_z). \tag{2}$$

To map the measurement points $\hat{\boldsymbol{x}}_{i,S}$ in the SCS to the corresponding points $\hat{\boldsymbol{x}}_{i,P}$ in the PCS, we apply a rigid transformation that consists of rotations and translations. The transformation is defined as

$$\hat{\boldsymbol{x}}_{i,P} = \boldsymbol{R}_Z(\theta_z)\boldsymbol{R}_Y(\theta_y)\boldsymbol{R}_X(\theta_x)\hat{\boldsymbol{x}}_{i,S} + [0, \delta_y, \delta_z]^T. \tag{3}$$

where $\boldsymbol{R}_X(\theta_x)$, $\boldsymbol{R}_Y(\theta_y)$, and $\boldsymbol{R}_Z(\theta_z)$ are 3D rotation matrices about the X-, Y-, and Z axes, respectively, and $[0, \delta_y, \delta_z]^T$ represents the translation vector. Given this transformation, the measurement points in the PCS align with the elliptical cross-section model of the pipe, enabling a more structured evaluation of the data.

We formulate the problem of estimating $\boldsymbol{\beta}$ as a non-linear least-squares fitting problem, which minimizes errors by fitting the sensor measurements to an elliptical cross-section model. The optimization minimizes the sum of squared residuals between the transformed points and the elliptical model of the pipe. The residual function, denoted as $r(\hat{\boldsymbol{x}}_{i,P}, \boldsymbol{\beta})$, evaluates the fit of each transformed point, $\hat{\boldsymbol{x}}_{i,P}$, to the ellipse defined by the parameters $D_{\max}$ and $D_{\min}$. The objective function for this optimization is expressed as

$$F(\boldsymbol{\beta}) = \sum_{i=1}^{N} r^2(\hat{\boldsymbol{x}}_{i,P}, \boldsymbol{\beta}). \tag{4}$$

To solve this non-linear least-squares problem, we employ iterative optimization algorithms that are widely used in non-linear parameter estimation. These include the gradient descent algorithm [23], the Gauss–Newton algorithm [24], and the Levenberg–Marquardt algorithm [25,26]. The gradient descent algorithm follows the steepest path in the opposite direction to the gradient with a step size called learning rate. A small learning rate leads to slow convergence while a large one incurs divergence. The Gauss–Newton method approximates the objective function as a quadratic function and computes a step that minimizes the quadratic function. It may not converge if the initial guess is far from the solution. The Levenberg–Marquardt algorithm combines these two algorithms by introducing the damping factor. Based on the damping factor, it acts like gradient descent for stability when far from the solution and acts like the Gauss–Newton model when close to the solution for faster convergence. Due to its advantages, we choose the Levenberg–Marquardt method as the optimization algorithm. This algorithm iteratively updates the parameters of $\boldsymbol{\beta}$ to minimize the residual errors, ensuring that the transformed points closely match the elliptical model of the pipe.

In the following sections, we define two types of residual functions and mathematically model their impacts on the estimation of robot pose and pipe diameter.

3.2. Analysis of Residual Asymmetry in C-EPD

In this section, we present the C-EPD scheme, which uses a canonical ellipse residual function to evaluate how well measurement points fit the elliptical model of the pipe. We mathematically analyze the residual asymmetry caused by the uneven treatment of random depth errors, leading to the potential overestimation of pipe diameter.

The canonical ellipse form, widely used to model elliptical shapes, is expressed as follows:

$$\frac{\hat{y}_P^2}{(D_{\max}/2)^2} + \frac{\hat{z}_P^2}{(D_{\min}/2)^2} = 1 \tag{5}$$

In the C-EPD framework, the residual function $r_c(\hat{\boldsymbol{x}}_{i,P}, \boldsymbol{\beta})$ measures the deviation of the point $\hat{\boldsymbol{x}}_{i,P}$ from the elliptic surface and is given by

$$r_c(\hat{\boldsymbol{x}}_{i,P}, \boldsymbol{\beta}) = \frac{\hat{y}_{i,P}^2}{(D_{\max}/2)^2} + \frac{\hat{z}_{i,P}^2}{(D_{\min}/2)^2} - 1 \tag{6}$$

The optimal C-EPD transformation parameters $\boldsymbol{\beta}^*_{C-EPD}$ minimize the objective function in (4), as follows:

$$\boldsymbol{\beta}^*_{C-EPD} = \arg\min_{\forall \boldsymbol{\beta}} \sum_{i=1}^{N} r_c^2(\hat{\boldsymbol{x}}_{i,P}, \boldsymbol{\beta}). \tag{7}$$

We analyze the residual asymmetry of the canonical ellipse function, focusing on its sensitivity to random depth errors. Given identical magnitudes of random errors, positive-error points tend to yield higher residuals than negative-error points. This imbalance introduces systematic overestimation of pipe diameters during optimization. We now explain and mathematically prove this asymmetry using a conceptual framework.

Figure 2 illustrates the canonical residual function in a scaled coordinate system where the ellipse is transformed into a unit circle. The transformation to a unit circle is a non-uniform scaling transformation where the scaling factors are different in each scaling direction. In general, the non-uniform scaling transformation distorts distances and shapes, e.g., from an ellipse to a circle. However, it preserves the relative distance along the same scaling direction. In Figure 2, the ground-truth, positive-error, and negative-error points lie in the same scaling direction; therefore, the relative error magnitudes between them are preserved. The scaling operation does not alter the order of the residual errors introduced by the random depth errors, ensuring that the asymmetry remains consistent. Additionally, by converting the ellipse to a circle, the effect of different eccentricities (varying shapes and degrees of elongation of the ellipse) is neutralized. This transformation enables a clearer visualization and interpretation of how positive- and negative-error points influence residual computations, emphasizing the estimation bias introduced by asymmetric error treatment in the canonical residual function.

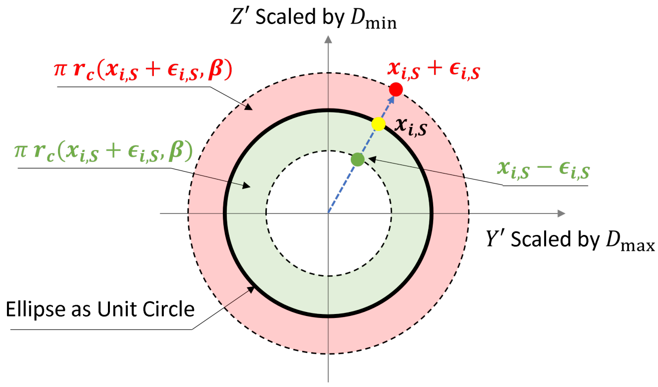

Figure 2. Conceptual representation of canonical ellipse residual function in coordinate system scaled by $D_{\max}$ and $D_{\min}$.

The scaled coordinate system maintains the geometric relationship by normalizing the axes based on the major-axis length ($D_{\max}$) and minor-axis length ($D_{\min}$). A point, $\hat{\boldsymbol{x}}_{i,P}$, in the PCS is transformed to $\tilde{\boldsymbol{x}}_{i,P}$ in the scaled coordinate system as follows:

$$\tilde{\boldsymbol{x}}_{i,P} = \boldsymbol{T}\hat{\boldsymbol{x}}_{i,P}, \tag{8}$$

where the transformation to the scaled system is defined by the matrix

$$\boldsymbol{T} = \begin{bmatrix} 1 & 0 & 0 \\ 0 & \frac{2}{D_{\max}} & 0 \\ 0 & 0 & \frac{2}{D_{\min}} \end{bmatrix}. \tag{9}$$

In the scaled system, the ellipse is represented as a unit circle, and the residual function simplifies to

$$r_c(\tilde{\boldsymbol{x}}_{i,P}, \boldsymbol{\beta}) = \tilde{y}_{i,P}^2 + \tilde{z}_{i,P}^2 - 1. \tag{10}$$

Multiplying this equation by π gives

$$\pi r_c(\tilde{\boldsymbol{x}}_{i,P}, \boldsymbol{\beta}) = \pi(\tilde{y}_{i,P}^2 + \tilde{z}_{i,P}^2) - \pi, \tag{11}$$

where the first term represents the area of the circle passing through the point $\tilde{\boldsymbol{x}}_{i,P}$, and the second term represents the area of the unit circle. The residual $\pi r_c(\tilde{\boldsymbol{x}}_{i,P}, \boldsymbol{\beta})$ corresponds to the shaded annular area between these two circles, as shown in Figure 2. This figure illustrates that the residual area for positive-error points (red region) is larger than that for negative-error points (green region) given the same magnitude of error, ϵ_i. This asymmetry causes a systematic estimation bias during optimization, favoring larger diameters to minimize errors.

Lemma 1 formalizes this observation by proving that the canonical residual function systematically assigns larger errors to positive-error points compared to negative-error points with identical error magnitudes.

Lemma 1 (Asymmetry in Canonical Residual Function). *For two measurement points, $\boldsymbol{x}_{i,S} + \boldsymbol{\epsilon}_{i,S}$ and $\boldsymbol{x}_{i,S} - \boldsymbol{\epsilon}_{i,S}$, where $|\boldsymbol{x}_{i,S} + \boldsymbol{\epsilon}_{i,S}| > |\boldsymbol{x}| > |\boldsymbol{x}_{i,S} - \boldsymbol{\epsilon}_{i,S}|$, the squared canonical residual function satisfies*

$$r_c^2(\boldsymbol{x}_{i,S} + \boldsymbol{\epsilon}_{i,S}, \boldsymbol{\beta}) > r_c^2(\boldsymbol{x}_{i,S} - \boldsymbol{\epsilon}_{i,S}, \boldsymbol{\beta}). \tag{12}$$

This result demonstrates that the canonical residual function penalizes positive errors more heavily than negative errors, leading to systematic overestimations of pipe diameters in (7).

Proof. To prove $r_c^2(\boldsymbol{x}_{i,S}+\boldsymbol{\epsilon}_{i,S},\boldsymbol{\beta}) > r_c^2(\boldsymbol{x}_{i,S}-\boldsymbol{\epsilon}_{i,S},\boldsymbol{\beta})$, we begin by evaluating the difference between the squared residuals: $r_c^2(\boldsymbol{x}_{i,S}+\boldsymbol{\epsilon}_{i,S},\boldsymbol{\beta}) - r_c^2(\boldsymbol{x}_{i,S}-\boldsymbol{\epsilon}_{i,S},\boldsymbol{\beta}) > 0$. Then, we expand $r_c^2(\boldsymbol{x}_{i,S}+\boldsymbol{\epsilon}_{i,S},\boldsymbol{\beta}) - r_c^2(\boldsymbol{x}_{i,S}-\boldsymbol{\epsilon}_{i,S},\boldsymbol{\beta})$ as follows:

$$\begin{aligned} r_c^2(\boldsymbol{x}_{i,S}+\boldsymbol{\epsilon}_{i,S},\boldsymbol{\beta}) - r_c^2(\boldsymbol{x}_{i,S}-\boldsymbol{\epsilon}_{i,S},\boldsymbol{\beta}) = \\ [r_c(\boldsymbol{x}_{i,S}+\boldsymbol{\epsilon}_{i,S},\boldsymbol{\beta}) + r_c(\boldsymbol{x}_{i,S}-\boldsymbol{\epsilon}_{i,S},\boldsymbol{\beta})] \cdot [r_c(\boldsymbol{x}_{i,S}+\boldsymbol{\epsilon}_{i,S},\boldsymbol{\beta}) - r_c(\boldsymbol{x}_{i,S}-\boldsymbol{\epsilon}_{i,S},\boldsymbol{\beta})] \end{aligned} \tag{13}$$

Denoting a transformed vector of $\boldsymbol{\epsilon}_{i,S}$ in the PCS by $\boldsymbol{\epsilon}_{i,P} = [\epsilon_{x,i,P}, \epsilon_{y,i,P}, \epsilon_{z,i,P}]^T$, the canonical residual functions for the positive and negative errors are expressed as

$$r_c(\boldsymbol{x}_{i,S}+\boldsymbol{\epsilon}_{i,S},\boldsymbol{\beta}) = \frac{(y_{i,P}+\epsilon_{y,i,P})^2}{(D_{\max}/2)^2} + \frac{(z_{i,P}+\epsilon_{z,i,P})^2}{(D_{\min}/2)^2} - 1, \tag{14}$$

and

$$r_c(\boldsymbol{x}_{i,S}-\boldsymbol{\epsilon}_{i,S},\boldsymbol{\beta}) = \frac{(y_{i,P}-\epsilon_{y,i,P})^2}{(D_{\max}/2)^2} + \frac{(z_{i,P}-\epsilon_{z,i,P})^2}{(D_{\min}/2)^2} - 1, \tag{15}$$

respectively. From geometry, the positive-error point $\boldsymbol{x}_{i,S}+\boldsymbol{\epsilon}_{i,S}$ lies outside the pipe, making $r_c(\boldsymbol{x}_{i,S}+\boldsymbol{\epsilon}_{i,S},\boldsymbol{\beta}) > 0$. Conversely, the negative-error point $\boldsymbol{x}_{i,S}-\boldsymbol{\epsilon}_{i,S}$ lies inside the pipe, yielding $r_c(\boldsymbol{x}_{i,S}-\boldsymbol{\epsilon}_{i,S},\boldsymbol{\beta}) < 0$. Consequently, the second term in the right-hand side (RHS) of (13) becomes positive, contributing to larger residuals for positive errors.

On the other hand, by substituting (14) and (15), the first term in the RHS of (13) is simplified as follows:

$$\begin{aligned} r_c(\boldsymbol{x}_{i,S}+\boldsymbol{\epsilon}_{i,S},\boldsymbol{\beta}) + r_c(\boldsymbol{x}_{i,S}-\boldsymbol{\epsilon}_{i,S},\boldsymbol{\beta}) = \\ 2\left(\frac{y_{i,P}^2}{(D_{\max}/2)^2} + \frac{z_{i,P}^2}{(D_{\min}/2)^2} - 1\right) + \left(\frac{\epsilon_{y,i,P}^2}{(D_{\max}/2)^2} + \frac{\epsilon_{z,i,P}^2}{(D_{\min}/2)^2}\right) \end{aligned} \tag{16}$$

Note that the first term in the RHS of (16) equals zero at the ground-truth point, while the second term is always positive due to the squared terms. Since both terms in (13) are positive, the expanded inequality $r_c^2(\boldsymbol{x}_{i,S}+\boldsymbol{\epsilon}_{i,S},\boldsymbol{\beta}) > r_c^2(\boldsymbol{x}_{i,S}-\boldsymbol{\epsilon}_{i,S},\boldsymbol{\beta})$ proves that positive errors incur larger residuals than negative errors, causing systematic overestimations in pipe diameter estimation. □

There is a relationship between pipe diameter, random depth error, and the estimation bias in the canonical ellipse residual function that can be inferred from (16). As the random depth error increases, the second term in (16) becomes larger. This behavior amplifies the asymmetry in $r_c(\hat{\boldsymbol{x}}_{i,S},\boldsymbol{\beta})$, resulting in a systematic estimation bias. Due to this asymmetry, the canonical ellipse residual function causes the optimization process to estimate larger diameters than the ground-truth values. Theorem 1 formally states that the optimal solution $\boldsymbol{\beta}^*_{C-EPD}$ in (7) produces overestimated pipe diameters $(\hat{D}_{\max}, \hat{D}_{\min})$ compared to the ground-truth diameters $(D_{\max}, D_{\min})$.

Theorem 1 (Diameter Estimation Bias). *Given zero-mean Gaussian random depth errors and the canonical ellipse residual function, the estimated diameters are systematically overestimated, i.e.,* $\hat{D}_{\max} > D_{\max}$ *and* $\hat{D}_{\min} > D_{\min}$.

Proof. At the optimal diameters $(\hat{D}\text{max}, \hat{D}\text{min})$, the objective function $F(\boldsymbol{\beta})$ in (4) satisfies the following conditions:

$$\frac{\partial F}{\partial \hat{D}_{\max}} = 0 \quad \text{and} \quad \frac{\partial F}{\partial \hat{D}_{\min}} = 0. \tag{17}$$

From (14) and (15), the partial derivatives with respect to $\hat{D}_{\max}$ and $\hat{D}_{\min}$ are computed by

$$\frac{\partial F}{\partial \hat{D}_{\max}} = -\frac{8}{\hat{D}^3_{\max}} \sum_{i=1}^{N} r_c(\boldsymbol{x}_{i,S} + \boldsymbol{\epsilon}_{i,S}, \boldsymbol{\beta}) \left(y_{i,P} + \epsilon_{y,i,P}\right)^2, \tag{18}$$

and

$$\frac{\partial F}{\partial \hat{D}_{\min}} = -\frac{8}{\hat{D}^3_{\min}} \sum_{i=1}^{N} r_c(\boldsymbol{x}_{i,S} + \boldsymbol{\epsilon}_{i,S}, \boldsymbol{\beta}) (z_{i,P} + \epsilon_{z,i,P})^2, \tag{19}$$

respectively.

We observe that the terms $\left(y_{i,P} + \epsilon_{y,i,P}\right)^2$ and $(z_{i,P} + \epsilon_{z,i,P})^2$ for positive-error points dominate over those for negative-error points due to their squared values. Furthermore, from Lemma 1, the residual function $r_c(\boldsymbol{x}_{i,S} + \boldsymbol{\epsilon}_{i,S}, \boldsymbol{\beta})$ associated with positive-error points is greater in magnitude than that of negative-error points.

Given that the random depth errors are modeled as zero-mean Gaussian distributions, the contributions from positive-error points dominate the optimization process. As a result, the optimizer compensates for the larger residuals by increasing the diameters $\hat{D}_{\max}$ and $\hat{D}_{\min}$ to reduce their impact, leading to $\hat{D}_{\max} > D_{\max}$ and $\hat{D}_{\min} > D_{\min}$. This systematic adjustment confirms the estimation bias in the canonical ellipse residual function. □

3.3. Analysis of Residual Symmetry in RU-EPD

To address the limitations of the C-EPD scheme caused by the asymmetry of the canonical ellipse residual function, we propose the RU-EPD scheme. This approach introduces a novel error-based residual function that ensures unbiased and accurate estimation under random depth errors. The proposed residual function evaluates the projected depth error in the YZ-plane of the PCS. Unlike the canonical approach, which indirectly measures deviations from the ellipse model, this function directly estimates the depth error itself, eliminating asymmetry.

Figure 3 illustrates the proposed residual function based on the distance between the measurement point $\hat{\boldsymbol{x}}_{i,P}$ and its ground truth $\boldsymbol{x}_{i,P}$ in the YZ-plane. The proposed residual function captures the difference in radial distances from the sensor origin $\boldsymbol{x}_{0,P}$ to the measured point $\hat{\boldsymbol{x}}_{i,P}$ and the intersection point $\boldsymbol{x}_{i,P}$. This formulation assigns negative values to negative-error points and positive values to positive-error points, inherently preserving the signed depth error and eliminating the estimation bias present in the C-EPD scheme. Then, the error-based residual function is formally defined as follows:

$$r_d(\hat{\boldsymbol{x}}_{i,P}, \boldsymbol{\beta}) = \sqrt{(\hat{y}_{i,P} - y_{0,P})^2 + (\hat{z}_{i,P} - z_{0,P})^2} - \sqrt{(y_{i,P} - y_{0,P})^2 + (z_{i,P} - z_{0,P})^2}. \tag{20}$$

The intersection point $\tilde{\boldsymbol{x}}_{i,P}$ is computed as the point where the ellipse model intersects the sensing line passing through the sensor origin $\boldsymbol{x}_{0,P}$ and the measurement point $\hat{\boldsymbol{x}}_{i,P}$. The parametric equation for this line is given by

$$\hat{y}_P = y_{0,P} + t(\hat{y}_{i,P} - y_{0,P}), \text{ and } \hat{z}_P = z_{0,P} + t(\hat{z}_{i,P} - z_{0,P}). \tag{21}$$

Substituting $\hat{y}_P$ and $\hat{z}_P$ into the ellipse Equation (5) yields a quadratic equation in t. The solution is given by

$$t = \frac{\sqrt{A - \frac{(z_{0,P}\hat{y}_{i,P} - y_{0,P}\hat{z}_{i,P})^2}{(D_{\max}/2)^2(D_{\min}/2)^2}} - \left(\frac{y_{0,P}(\hat{y}_{i,P} - y_{0,P})}{(D_{\max}/2)^2} + \frac{z_{0,P}(\hat{z}_{i,P} - z_{0,P})}{(D_{\min}/2)^2}\right)}{A}, \quad (22)$$
$$\text{where } A = \frac{(\hat{y}_{i,P} - y_{0,P})^2}{(D_{\max}/2)^2} + \frac{(\hat{z}_{i,P} - z_{0,P})^2}{(D_{\min}/2)^2}.$$

By substituting the line equation in (21) into (20), the error-based residual function r_d is further simplified as follows:

$$r_d(\hat{\boldsymbol{x}}_{i,S}, \boldsymbol{\beta}) = (1 - t)\sqrt{(\hat{y}_{i,P} - y_{0,P})^2 + (\hat{z}_{i,P} - z_{0,P})^2}. \quad (23)$$

Finally, the optimal RU-EPD parameters $\boldsymbol{\beta}^*_{RU-EPD}$ are obtained by minimizing the following objective function:

$$\boldsymbol{\beta}^*_{RU-EPD} = \arg\min_{\forall \boldsymbol{\beta}} \sum_{i=1}^{N} r_d^2(\hat{\boldsymbol{x}}_{i,P}, \boldsymbol{\beta}). \quad (24)$$

Unlike the canonical approach, the residual function r_d is inherently symmetric with respect to random depth errors. If the diameter components of $\boldsymbol{\beta}$ match the ground truths, the intersection point $\tilde{\boldsymbol{x}}_{i,P}$ coincides with the ground-truth point $\boldsymbol{x}_{i,P}$. In this case, r_d directly reflects the true random depth error magnitude in the YZ-plane, preserving the signed nature of the errors. As a result, r_d eliminates the estimation bias issue observed in the canonical residual function. Theorem 2 formally establishes that the ground-truth diameters $D_{\max}$ and $D_{\min}$ minimize the cost function when using the error-based residual function r_d.

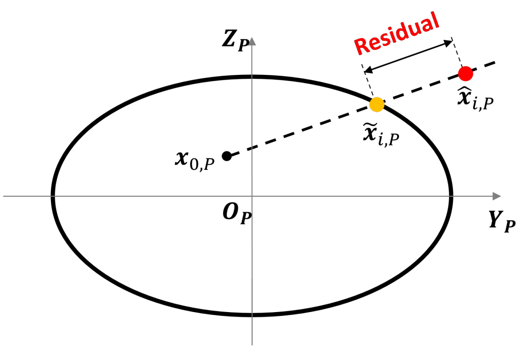

Figure 3. Unbiased residual based on distance between measurement point $\hat{\boldsymbol{x}}_{i,P}$ and its ground truth $\tilde{\boldsymbol{x}}_{i,P}$ in YZ-plane in PCS.

Theorem 2 (**Unbiased Diameter Estimation with Error-based Residual Function**). *With zero-mean Gaussian random depth errors and the error-based residual function, the ground-truth diameters $D_{\max}$ and $D_{\min}$ minimize the cost function.*

Proof. We assume that there is another solution, $\hat{\boldsymbol{\beta}}$, containing $D_{\max} + \gamma$ and $D_{\min} + \delta$ which yields a lower cost function than $\boldsymbol{\beta}^*_{RU-EPD}$, which contains $D_{\max}$ and $D_{\min}$. For alternative diameters, the residual function $r_d(\hat{\boldsymbol{x}}_{i,P}, \hat{\boldsymbol{\beta}})$ can be represented by

$$r_d(\hat{\boldsymbol{x}}_{i,P}, \hat{\boldsymbol{\beta}}) = r_d(\hat{\boldsymbol{x}}_{i,P}, \boldsymbol{\beta}^*_{RU-EPD}) + \alpha_i, \quad (25)$$

where α_i is the difference between these two residual functions. Then, the objective function becomes

$$F(\hat{\boldsymbol{\beta}}) = \sum_{i=1}^{N}(r_d(\hat{\boldsymbol{x}}_{i,P}, \hat{\boldsymbol{\beta}}) + \alpha_i)^2 = \sum_{i=1}^{N} r_d^2(\hat{\boldsymbol{x}}_{i,P}, \hat{\boldsymbol{\beta}}) + 2\sum_{i=1}^{N} r_d(\hat{\boldsymbol{x}}_{i,P}, \hat{\boldsymbol{\beta}})\alpha_i + \sum_{i=1}^{N}(\alpha_i)^2. \tag{26}$$

Because the random depth error follows a zero-mean Gaussian distribution, the signed residuals of negative-error points cancel out those of positive-error points. Hence, the second term approaches zero. The third term, being strictly positive, increases the objective function under the alternative diameters in $\hat{\boldsymbol{\beta}}$. As a result, the objective function for the ground-truth diameters $D_{\max}$ and $D_{\min}$ is strictly lower than that for any other diameters. Therefore, the ground-truth diameters $D_{\max}$ and $D_{\min}$ minimize the objective function based on the error-based residual function. Note that, even when the random depth error is only symmetric but does not follow a zero-mean Gaussian distribution, the second term still approaches zero and the proof also holds. □

Since the ground-truth diameter $D_{\max}$ and $D_{\min}$ minimize the cost function in RU-EPD, the pose $(\theta_x, \theta_y, \theta_z, \delta_y, \delta_z)$ also has a high possibility of converging to the ground truth to keep the cost function minimized. On the other hand, the ground-truth diameter does not minimize the cost function in C-EPD, which allows other inaccurate diameters and poses to become solutions in C-EPD. As a result, RE-EPD is more robust and consistent than C-EPD besides eliminating the estimation bias.

4. Numerical Results

In this section, we compare the proposed RU-EPD scheme against the baseline C-EPD scheme using both simulated and experimental data. We first evaluate the pipe diameter estimation and robot pose estimation performance based on the simulation data. Then, we evaluate the performance with the real experimental data collected in 20″ pipelines.

4.1. Estimation Results Based on Simulation Data

To compare RU-EPD and C-EPD, we collected the simulation data generated by a self-developed simulation tool. It generated the measurement points of a 3D ToF sensor mounted in front of a robot on a pipe inner surface. The reference sensor model was the Helios2 3D ToF camera [17] with a resolution of 640 × 480 and a FoV of 69° × 51°. The pipe thickness was 12 mm. For each simulation, 100 random poses of the sensor were generated where the ranges were as follows: roll angle range, $[-180, 180]$; pitch and yaw angle range, $[-5°, 5°]$; and Y- and Z-displacement range, $[-50, 50]$ mm. Data points within 6 m were used for estimation.

4.1.1. Pipe Diameter Estimation

In this section, we evaluate the accuracy of pipe diameter estimation in terms of the major axis and minor axis. We first discuss the effect of the sensor depth error which was the main cause of the overestimation of pipe diameter. Then, the effect of pipe diameter, the secondary factor that contributed to the overestimation, is also considered. We focus on the estimation bias and the estimation error range. The estimation bias is defined as the mean of the estimation error. It evaluates if there was a bias in the estimation. The estimation error range is defined as the difference between the maximum and the minimum estimation errors. It indicates the consistency of the estimation.

Figure 4 shows the major-axis and minor-axis estimation results with different sensor depth errors, σ_ϵ, from 0.01 to 0.05 m. The lines and circle markers represent the estimation bias while the error bar represents the estimation error range. First, C-EPD exhibited a significant overestimation of both the major and minor axes, with the estimation bias reaching up to 6.67 mm. This estimation bias was not accurate enough to estimate the thickness as well as the deformation of the pipe. It led to a wrong indication of pipe integrity.

In contrast, RU-EPD maintained the estimation bias below 0.10 mm, demonstrating an over 66 times higher accuracy. Second, the estimation error range increased with the sensor depth error in both C-EPD and RU-EPD. In the worst case, the estimation error range could be 3.02 mm with C-EPD. In contrast, RU-EPD maintained the estimation error range below 1.12 mm, approximately 2.5 times lower than that for C-EPD. This means that RU-EPD not only eliminated the estimation bias but also ensured robust and consistent estimations, irrespective of the robot pose.

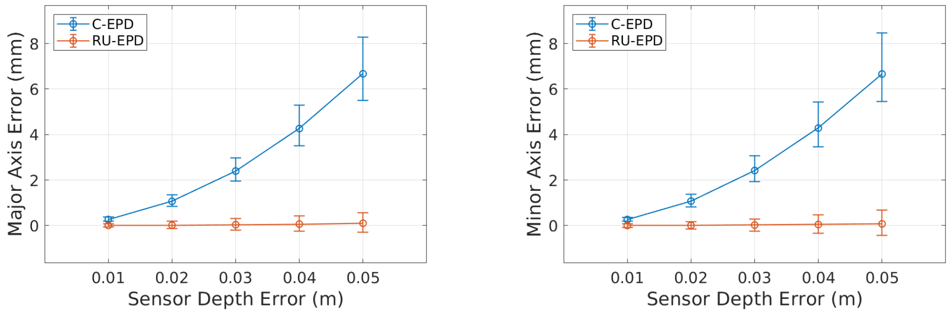

(**a**) Major-axis error. (**b**) Minor-axis error.

Figure 4. Comparison of pipe diameter estimation errors between C-EPD and RU-EPD under varying sensor depth errors.

Next, we evaluated the major axis and minor axis with different diameters from 16″ to 30″. The sensor depth error was set to 0.03 m. Figure 5 shows the major-axis and minor-axis estimation results. With C-EPD, the estimation bias was more severe with smaller pipe diameters, which agrees with our inference from (16). The estimation bias of C-EPD was up to 3.01 mm while the one of RU-EPD was as small as 0.05 mm. Additionally, the estimation error range of C-EPD also increased with smaller pipe diameters while it was almost constant and smaller in RU-EPD. In general, RU-EPD produced robust and unbiased pipe diameter estimations regardless of the sensor depth error and pipe diameter.

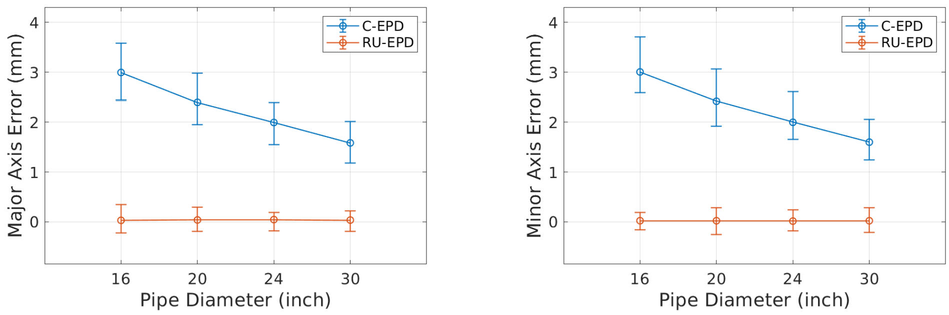

(**a**) Major-axis error. (**b**) Minor-axis error.

Figure 5. Comparison of pipe diameter estimation errors between C-EPD and RU-EPD under varying pipe diameters.

4.1.2. Robot Pose Estimation

We evaluated pose estimation performance, including roll, pitch, yaw, Y-displacement, and Z-displacement, under varying sensor depth errors. Figure 6 shows the results of the pose estimation. We can see that all five pose elements had similar trends with the sensor depth error. RU-EPD had no estimation bias, while there was a small estimation bias with C-EPD. The estimation error range of both C-EPD and RU-EPD increased as the sensor depth increased, but RU-EPD achieved a much smaller estimation error range. RU-EPD maintained the estimation error range of pitch and yaw accuracy as 0.12° while the one of the Y- and Z-displacement error was 2.15 mm. The roll angle error was relatively higher than that of the pitch and yaw but the estimation error range was still within 8.28°. These results confirm that RU-EPD not only eliminated estimation bias but also delivered consistent performance, making it suitable for in-pipe navigation systems.

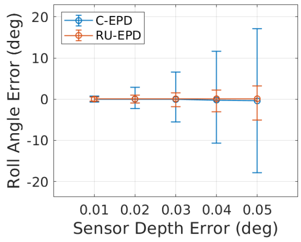

(**a**) Roll angle error.

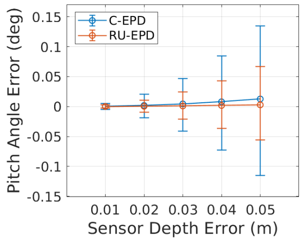

(**b**) Pitch angle error.

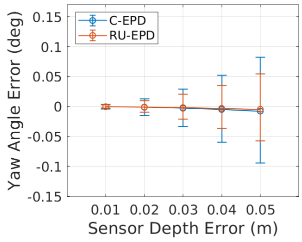

(**c**) Yaw angle error.

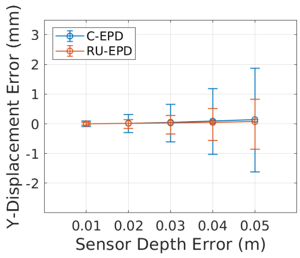

(**d**) Y-displacement error.

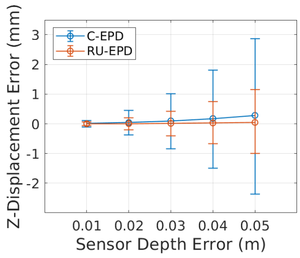

(**e**) Z-displacement error.

Figure 6. Robot pose estimation errors of C-EPD and RU-EPD across different sensor depth errors.

4.1.3. Processing Time

In this section, we discuss the processing time of RU-EPD and C-EPD with different input sizes from 10^2 to 10^5 points and evaluate the effect of the input sizes in terms of diameter estimation. Figure 7 shows the results of processing time on the PC with CPU Ryzen 9 5900x (3.7 GHz) and 48 GB of RAM. The processing time of RU-EPD and C-EPD was almost similar for all input sizes. The processing time increased with the input size. At the highest input size, the average processing time was about 0.54 s for both RU-EPD and C-EPD and did not exceed 1.1 s. It is suitable for post-processing systems where data are processed on a PC after inspection. For the input size 10^3 and below, the processing time did not exceed 0.03 s, which is suitable for real-time systems. On the other hand, Figure 8 shows the major- and minor-axis errors. The estimation error with both RU-EPD and C-EPD increased as the input size was reduced. However, RU-EPD still produced unbiased estimations compared to C-EPD. At 10^3, RU-EPD still kept the estimation error below 3.4 mm, which is acceptable in real-time systems.

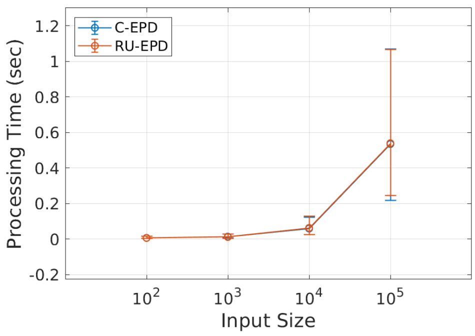

Figure 7. Comparison between processing time of C-EPD and RU-EPD under varying input sizes.

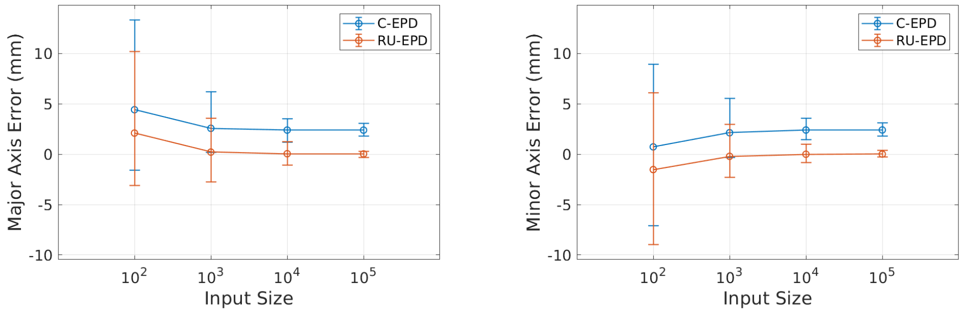

(**a**) Major-axis error. (**b**) Minor-axis error.

Figure 8. Comparison of pipe diameter estimation errors between C-EPD and RU-EPD under varying input sizes.

4.2. Estimation Results Based on Experimental Data

In this section, we evaluate the performance of C-EPD and RU-EPD on the real data collected using a Helios2 3D ToF camera on a 20″ pipeline. Figure 9 shows the robot and pipeline used in the experiment. The Helios2 3D ToF camera was equipped in front of the robot. A PC was also installed to control and store the measurement data from the camera. The experiment pipeline consisted of 4 straight pipes, one elbow, and one T-junction. The robot's trajectory in the pipeline is marked with the red arrows in Figure 9b. Due to physical constraints in the pipeline, data collection focused on two straight sections (11.9 T and 12.7 T), with 11.9 T and 12.7 T indicating that the nominal pipe thickness was 11.9 and 12.7 mm, respectively. In each pipe, we collected 50 frames from the Helios2 3D ToF camera. Figure 10 shows an example of measurement data from the Helios2 3D ToF camera. To remove the outliers, we only kept the points within $[0.5, 2]$ m for estimation. Additionally, we calibrated the Helios2 3D ToF camera to remove the depth bias using the approach in [27]. In this approach, the calibration information included correction offsets which were precomputed based on multiple frames collected in pipes with known diameters. The frames were first aggregated to remove random depth errors; then, the offsets from points in the aggregated frames to the pipe surface with a known diameter were used as the correction offsets. Calibration information was computed and stored in a lookup table separately for different pose and intensity intervals to address their diversities. Since the ground-truth pose could not be measured, we only evaluated the diameter estimation.

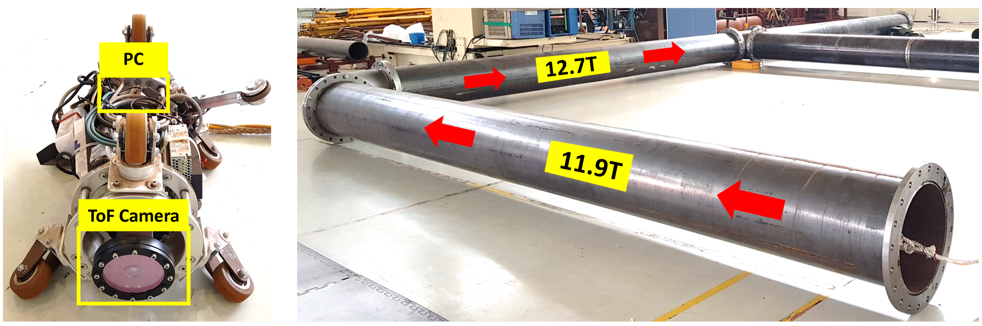

(**a**) Robot with ToF camera. (**b**) Experimental pipeline.

Figure 9. Experimental robot and pipeline.

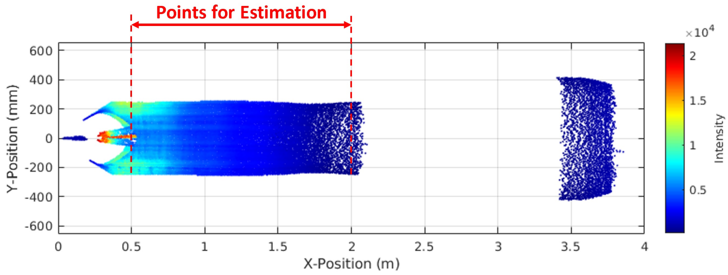

Figure 10. Measurement data collected by Helios2 3D ToF camera.

Figure 11 shows the estimation results of the major axis and minor axis in the 11.9 T and 12.7 T pipes. We can see a similar trend in both pipes. There were several samples where C-EPD estimated a very high major axis compared to the nominal diameter. The minor axis estimation of C-EPD was approximately around the nominal diameter. On the other hand, the major axis with RU-EPD was much more consistent and always smaller than the one with C-EPD. Most of the minor axis estimation in RU-EPD was below the nominal diameter.

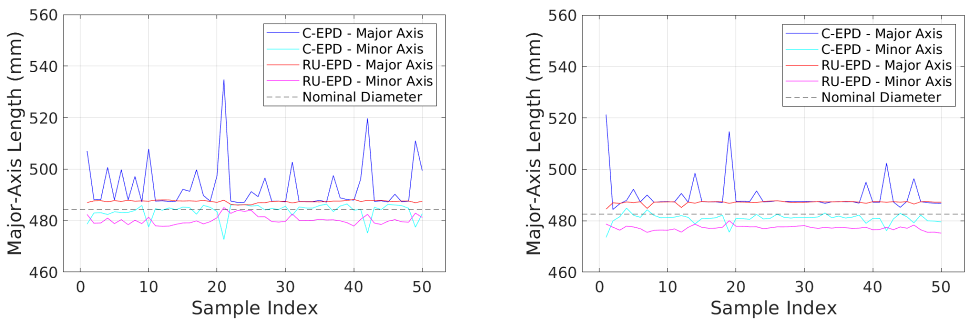

(**a**) 11.9 T. (**b**) 12.7 T.

Figure 11. Major-axis and minor-axis estimation of C-EPD and RU-EPD for 11.9 T and 12.7 T pipes.

Figure 12 shows the estimation errors of the major axis, minor axis, and mean diameter in the 11.9 T and 12.7 T pipes. Since the major axis error was positive and high with C-EPD and the minor axis error was small, it resulted in a clear estimation bias in the mean diameter as high as 4.2 mm. On the other hand, the major- and minor-axis errors with RU-EPD had opposite signs and had approximately the same value. Therefore, it led to an almost negligible estimation bias in the mean diameter of at most 0.46 mm, which was nine times smaller than that of C-EPD. We can also see that the estimation error range was very high with C-EPD. The estimation error range of the diameter was 18.16 mm in the 11.9 T pipe and 15.24 mm in the 12.7 T pipe. On the other hand, the estimation error range of the diameter with RU-EPD was at most 3.62 mm, which was at least four times smaller. The experiment results also confirm that RU-EPD had almost no estimation bias and robust estimation.

These results demonstrate the superior performance of RU-EPD over C-EPD in both the simulated and experimental scenarios. RU-EPD effectively mitigates estimation bias and delivers robust estimations, making it a promising solution for pipeline inspection tasks.

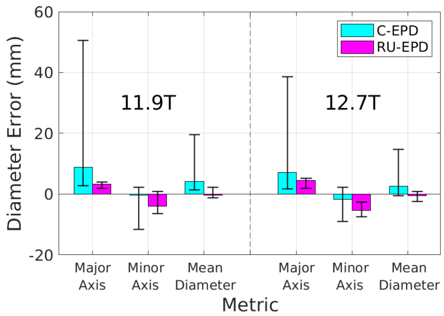

Figure 12. Average major-axis, minor-axis, and mean-diameter error of C-EPD and RU-EPD in 11.9 T and 12.7 T pipes.

5. Conclusions

This paper addressed the challenge of accurately estimating the pose of ILI robots and pipe diameters using a 3D ToF sensor. We identified and analyzed the limitations of the C-EPD scheme, highlighting its estimation bias due to the random depth errors of the 3D ToF sensor. To address these issues, we proposed the RU-EPD scheme. RU-EPD uses an error-based residual function to eliminate estimation bias and improve accuracy. Simulations and experiments demonstrated that RU-EPD significantly outperformed C-EPD, achieving robust and unbiased estimations under varying conditions. Specifically, RU-EPD achieved an at least six times lower estimation bias and a 2.5 times smaller estimation error range in pipe diameter and about a 2 times smaller estimation error range in pose estimation. RU-EPD enabled the identification of the change in thickness among the pipes. In summary, RU-EPD offers a practical and reliable solution for pipeline inspection. Future work will explore three key areas: (1) enhancing the robustness of RU-EPD through theoretical convergence analysis, (2) developing an efficient point sampling scheme for real-time estimation, and (3) extending RU-EPD to handle complex pipeline geometries such as elbows and T-junctions. In these geometries, RU-EPD needs to adapt to the torus model or a combination of ellipse, plane, and torus models.

Author Contributions: Conceptualization, H.-H.N. and H.-Y.J.; Data curation, H.-H.N., J.-H.P., J.-J.K. and K.Y.; Formal analysis, H.-H.N. and H.-Y.J.; Funding acquisition, D.-K.K. and H.-Y.J.; Investigation, H.-H.N. and H.-Y.J.; Methodology, H.-H.N. and H.-Y.J.; Project administration, D.-K.K. and H.-Y.J.; Resources, H.-H.N. and H.-Y.J.; Software, H.-H.N., J.-H.P., J.-J.K. and K.Y.; Supervision, D.-K.K. and H.-Y.J.; Validation, H.-H.N., J.-H.P., J.-J.K. and K.Y.; Visualization, H.-H.N.; Writing—original draft, H.-H.N.; Writing—review and editing, H.-H.N. and H.-Y.J. All authors have read and agreed to the published version of the manuscript.

Funding: This research was supported by the "Development of Next Generation Pipeline Robot Technology for the Long-Distance Inspection of the Low Pressure of Gas Pipeline" (RD 2019-0251) research project from Korea Gas Corporation (KOGAS).

Data Availability Statement: The original contributions presented in this study are included in the article. Further inquiries can be directed to the corresponding author.

Conflicts of Interest: The authors declare no conflicts of interest.

References

1. Ab Rashid, M.Z.; Mohd Yakub, M.F.; Zaki bin Shaikh Salim, S.A.; Mamat, N.; Syed Mohd Putra, S.M.; Roslan, S.A. Modeling of the in-pipe inspection robot: A comprehensive review. *Ocean Eng.* **2020**, *203*, 107206. [CrossRef]
2. Ma, Q.; Tian, G.; Zeng, Y.; Li, R.; Song, H.; Wang, Z.; Gao, B.; Zeng, K. Pipeline In-Line Inspection Method, Instrumentation and Data Management. *Sensors* **2021**, *21*, 3862. [CrossRef] [PubMed]
3. Abdellatif, F.; Alrasheed, A.J.; Felemban, A.; Al Brahim, A.; Jifri, H.; Abdelkader, M.; Ahmed, S.; Shamma, J.S. FalconScan: A hybrid UAV-crawler system for NDT inspection of elevated pipes in industrial plants. *Mechatronics* **2024**, *103*, 103239. [CrossRef]

4. Parlak, B.O.; Yavasoglu, H.A. A Comprehensive Analysis of In-Line Inspection Tools and Technologies for Steel Oil and Gas Pipelines. *Sustainability* **2023**, *15*, 2783. [CrossRef]
5. Kazeminasab, S.; Sadeghi, N.; Janfaza, V.; Razavi, M.; Ziyadidegan, S.; Banks, M.K. Localization, Mapping, Navigation, and Inspection Methods in In-Pipe Robots: A Review. *IEEE Access* **2021**, *9*, 162035–162058. [CrossRef]
6. Kim, J.; Muramatsu, M.; Murata, Y.; Suga, Y. Omnidirectional vision-based ego-pose estimation for an autonomous in-pipe mobile robot. *Adv. Robot.* **2007**, *21*, 441–460. [CrossRef]
7. Painumgal, U.V.; Thornton, B.; Uray, T.; Nose, Y. Positioning and control of an AUV inside a water pipeline for non-contact in-service inspection. In Proceedings of the 2013 OCEANS—San Diego, San Diego, CA, USA, 23–27 September 2013; pp. 1–10.
8. Dehghan Tezerjani, A.; Mehrandezh, M.; Paranjape, R. 4-DOF pose estimation of a pipe crawling robot using a Collimated Laser, a conic mirror, and a fish-eye camera. In Proceedings of the 2014 Southwest Symposium on Image Analysis and Interpretation, San Diego, CA, USA, 6–8 April 2014; pp. 45–48.
9. Hosseinzadeh, S.; Jackson, W.; Zhang, D.; McDonald, L.; Dobie, G.; West, G.; MacLeod, C. A Novel Centralization Method for Pipe Image Stitching. *IEEE Sens. J.* **2021**, *21*, 11889–11898. [CrossRef]
10. Buschinelli, P.; Pinto, T.; Silva, F.; Santos, J.; Albertazzi, A. Laser Triangulation Profilometer for Inner Surface Inspection of 100 millimeters (4”) Nominal Diameter. *J. Phys. Conf. Ser.* **2015**, *648*, 012010. [CrossRef]
11. Jin, L.; Miyatsu, N.; Kondoh, E.; Gelloz, B.; Kanazawa, N.; Yoshizawa, T. Measurement of diameter of cylindrical openings using a disk beam probe. *Opt. Rev.* **2018**, *25*, 656–662. [CrossRef]
12. Hansen, P.; Alismail, H.; Rander, P.; Browning, B. Monocular visual odometry for robot localization in LNG pipes. In Proceedings of the 2011 IEEE International Conference on Robotics and Automation, Shanghai, China, 9–13 May 2011; pp. 3111–3116.
13. Hansen, P.; Alismail, H.; Rander, P.; Browning, B. Visual mapping for natural gas pipe inspection. *Int. J. Robot. Res.* **2015**, *34*, 532–558. [CrossRef]
14. Shang, Z.; Shen, Z. Single-pass inline pipeline 3D reconstruction using depth camera array. *Autom. Constr.* **2022**, *138*, 104231. [CrossRef]
15. Yang, L.; Zhou, F.; Li, X.; Zhang, W.; Liu, Y.; Tan, H. 3-D Vision Measurement System and Method for Small-Diameter Pipeline. *IEEE Trans. Instrum. Meas.* **2024**, *73*, 1–11. [CrossRef]
16. OS0 Lidar Sensor. Available online: https://ouster.com/products/hardware/os0-lidar-sensor (accessed on 23 December 2024).
17. Helios2 3D Time-of-Flight (ToF) Camera. Available online: https://thinklucid.com/helios-time-of-flight-tof-camera/?srsltid=AfmBOor-Bj7TaCRf95rdjyes21Nju8Kdsbykw93sBLzzUcQtn-NrFDHO (accessed on 23 December 2024).
18. Hansard, M.; Lee, S.; Choi, O.; Horaud, R. *Time of Flight Cameras: Principles, Methods, and Applications*; Springer: London, UK, 2012; p. 95. [CrossRef]
19. Kuznetsova, A.; Rosenhahn, B. On calibration of a low-cost time-of-flight camera. In *Computer Vision—ECCV 2014 Workshops*; Lecture Notes in Computer Science; Springer: Cham, Switzerland, 2015; Volume 8925, pp. 415–427. [CrossRef]
20. He, Y.; Liang, B.; Zou, Y.; He, J.; Yang, J. Depth errors analysis and correction for time-of-flight (ToF) cameras. *Sensors* **2017**, *17*, 92. [CrossRef] [PubMed]
21. Fang, Y.J.; Wang, X.; Sun, Z.B.; Zhang, K.; Su, B.H. Study of the depth accuracy and entropy characteristics of a ToF camera with coupled noise. *Opt. Lasers Eng.* **2020**, *128*, 106001. [CrossRef]
22. Li, M.; Feng, X.; Hu, Q. 3D laser point cloud-based geometric digital twin for condition assessment of large diameter pipelines. *Tunn. Undergr. Space Technol.* **2023**, *142*, 105430. [CrossRef]
23. Ruder, S. An overview of gradient descent optimization algorithms. *arXiv* **2016**, arXiv:1609.04747.
24. Hartley, H.O. The modified Gauss-Newton method for the fitting of non-linear regression functions by least squares. *Technometrics* **1961**, *3*, 269–280. [CrossRef]
25. Levenberg, K. A method for the solution of certain non-linear problems in least squares. *Q. Appl. Math.* **1944**, *2*, 164–168. [CrossRef]
26. Marquardt, D.W. An algorithm for least-squares estimation of nonlinear parameters. *J. Soc. Ind. Appl. Math.* **1963**, *11*, 431–441. [CrossRef]
27. Park, J.H.; Nguyen, H.H.; Kim, J.J.; Yoo, K.; Yoo, H.R.; Kim, D.K.; Jeong, H.Y. Pipeline Diameter Estimation based on ToF Camera. 2025, *Preprints*.